Solid-State Batteries

International Edition: DOI: 10.1002/anie.201914478
German Edition: DOI: 10.1002/ange.201914478

Enhanced Surface Interactions Enable Fast Li^+ Conduction in Oxide/Polymer Composite Electrolyte

Nan Wu, Po-Hsiu Chien, Yumin Qian, Yutao Li, Henghui Xu, Nicholas S. Grundish, Biyi Xu, Haibo Jin, Yan-Yan Hu, Guihua Yu, and John B. Goodenough**

Abstract: *Li^+-conducting oxides are considered better ceramic fillers than Li^+-insulating oxides for improving Li^+ conductivity in composite polymer electrolytes owing to their ability to conduct Li^+ through the ceramic oxide as well as across the oxide/polymer interface. Here we use two Li^+-insulating oxides (fluorite $Gd_{0.1}Ce_{0.9}O_{1.95}$ and perovskite $La_{0.8}Sr_{0.2}Ga_{0.8}Mg_{0.2}O_{2.55}$) with a high concentration of oxygen vacancies to demonstrate two oxide/poly(ethylene oxide) (PEO)-based polymer composite electrolytes, each with a Li^+ conductivity above 10^{-4} S cm^{-1} at 30 °C. Li solid-state NMR results show an increase in Li^+ ions (>10 %) occupying the more mobile A2 environment in the composite electrolytes. This increase in A2-site occupancy originates from the strong interaction between the O^{2-} of Li-salt anion and the surface oxygen vacancies of each oxide and contributes to the more facile Li^+ transport. All-solid-state Li-metal cells with these composite electrolytes demonstrate a small interfacial resistance with good cycling performance at 35 °C.*

Introduction

Development of low-cost and safe rechargeable Li-ion batteries with a high energy density and a long cycling life is of great importance to meet the increasing requirements of different energy-storage applications such as all-electric vehicles (EVs).[1] However, the flammable and toxic liquid organic electrolytes in commercial rechargeable Li-ion batteries react with a metallic Li anode and the high-voltage cathodes to form an unstable solid electrolyte interphase (SEI) layer that reduces the cycle life of the battery.[1a,2] All-solid-state Li-metal batteries having a thin Li^+-conducting solid electrolyte and a high voltage/capacity cathode are much safer and have a higher energy density than the conventional rechargeable Li-ion batteries with a liquid organic electrolyte.[3] These enhanced properties of the solid-state battery architecture are owing to the ability to plate lithium on the Li-metal anode without lithium-dendrite formation. Li^+ solid electrolytes (including inorganic, polymer and inorganic/polymer composite materials) are still not competitively producible on a commercial scale because it is still quite challenging to develop a thin, low-cost solid electrolyte membrane with a high Li^+ conductivity with the following critical properties: a small interfacial resistance, a good chemical stability with electrodes, a large electrochemical window, and a strong inhibition of lithium-dendrite formation at a high current density.[3]

Inorganic oxide (e.g., Ga/Ta-doped garnet $Li_7La_3Zr_2O_{12}$),[4] sulfide (e.g., argyrodite Li_6PS_5Cl),[5] and halide (e.g., Li_3YCl_6)[6] electrolytes, with a high room-temperature Li^+ conductivity above 10^{-3} S cm^{-1} have been identified. However, large interfacial resistance with electrodes, instability with Li-metal anode, and the small critical current density at which the lithium dendrites penetrate the solid electrolyte and short circuit the cell limit the application of inorganic electrolytes in all-solid-state Li-metal batteries.[7] Moreover, these fragile inorganic electrolytes usually have a thickness above 200 μm, which significantly reduces the rate performance and energy density of the battery. Compared with the fragile inorganic solid electrolytes, solid polymer electrolytes such as poly(ethylene oxide) (PEO) and polyacrylonitrile (PAN) are flexible and have better interfacial contact with different electrodes than the inorganic electrolytes, which reduces the interfacial resistances of the batteries.[8] However, these solid polymer electrolytes usually have a low room-temperature Li^+ conductivity around 10^{-6} S cm^{-1} and a small Li^+ transference number about 0.2, which increases the overpotential of the batteries and limits the battery cycling temperatures to about 60 °C.[9]

Inorganic/polymer composite electrolytes with Li^+ insulating (e.g., nano-Al_2O_3)[10] or Li^+ conducting materials (e.g., Li_3N,[11] garnet $Li_7La_3Zr_2O_{12}$,[12] and perovskite $Li_{0.33}La_{0.56}TiO_3$[13]) as fillers have much higher Li^+ conductivities than those of polymer electrolytes at room temperature because of (1) the increase in concentration of Li^+-conducting amorphous polymer phase, (2) a new Li^+ transport path is

[*] N. Wu, H. Jin
Beijing Key Laboratory of Construction Tailorable Advanced Functional Materials and Green Applications, School of Materials Science & Engineering, Beijing Institute of Technology
Beijing 100081 (P. R. China)
N. Wu, Y. Qian, Y. Li, H. Xu, N. S. Grundish, B. Xu, G. Yu, J. B. Goodenough
Materials Science and Engineering Program and Texas Materials Institute, The University of Texas at Austin
Austin, TX 78712 (USA)
E-mail: lytthu@utexas.edu
jgoodenough@mail.utexas.edu
P.-H. Chien, Y.-Y. Hu
Center of Interdisciplinary Magnetic Resonance, National High Magnetic Field Laboratory
1800 East Paul Dirac Drive, Tallahassee, FL 32310 (USA)
Y.-Y. Hu
Department of Chemistry and Biochemistry, Florida State University
Tallahassee, FL 32306 (USA)
Supporting information and the ORCID identification number(s) for the author(s) of this article can be found under https://doi.org/10.1002/anie.201914478.

introduced on the inorganic materials/polymer interface, and (3) the Li^+ conduction in the Li^+ conducting inorganic materials. However, the complex Li^+ conduction mechanisms of these composite electrolytes are unclear; the Li^+ transfer in the polymer, on the inorganic/polymer interface, and across the inorganic materials (if they are Li^+ conducting) depends on the material, particle size, concentration, morphology, and distribution of the inorganic filler.[14] The thermal history, testing temperature, and residual organic solvents of the composite electrolytes also significantly influence their Li^+ conductivities. Owing to the rapid development of fast Li^+ conducting inorganic materials over the past several years, there has been a strong focus on Li^+-conducting inorganic materials/polymer composite electrolytes. At low to moderate loadings, these composite electrolytes are reported to have similar Li^+ conductivities as composite electrolytes with the Li^+-insulating-oxide fillers. High concentration of Li^+-conducting inorganic materials in the composite drastically hinders Li^+ transport, and the total Li^+ conductivity of the composite electrolyte is reduced.[15] The contribution of Li^+ conduction across the Li^+ conducting inorganic materials seems to be negligible when the isolated inorganic particles inside the composite do not form a suitable percolation network for Li^+ transfer, causing the Li^+ conductivity to be dominated by the low Li^+ conductivity of the polymer. Therefore, changing the local Li^+ environments to activate more mobile Li^+ in the polymer by adding inorganic filler materials that have a strong interaction with the polymer electrolytes should be a useful strategy to improve the Li^+ conductivity of the composite electrolytes and the Li^+ transfer within the polymers.

Polymer electrolytes with dissolved Li-salts interact with the ceramic fillers through surface interactions; increasing the surface defects of the fillers could modify the polymer/Li-salts interaction, Li^+ local environment, and the activation energy for Li^+ transport. To explore this possibility, we introduce two commercial Li^+-insulating oxides fluorite $Gd_{0.1}Ce_{0.9}O_{1.95}$ (GDC) and perovskite $La_{0.8}Sr_{0.2}Ga_{0.8}Mg_{0.2}O_{2.55}$ (LSGM) as a ceramic filler to the poly(ethylene oxide) (PEO)-based polymer; the oxygen vacancies $(V_O^{\bullet\bullet})$ in bulk and on the particle surface of these two materials should increase the interaction between the surface of oxides and the anion of the Li-salt in the polymer, promoting the mobility of Li^+ ions and enhancing the Li^+ conductivity of the composite electrolyte above 10^{-4} S cm^{-1} at 30 °C. Density functional calculations (DFT) show the formation of a bond between the $TFSI^-$ anion of the Li-salt and the surface of the inorganic filler. The fluorite GDC showed a much stronger interaction with the $TFSI^-$ anions than the perovskite LSGM. ^{7}Li relaxation time nuclear magnetic resonance (NMR) measurements confirm the existence of two different local Li^+ environments in the composite polymer electrolytes (designated A1 and A2). The distribution of Li^+ in the A1 and A2 sites changes with the introduction of GDC or LSGM. When the Li^+ population in the mobile A2 environment increases, the room temperature Li^+ conductivity of the composite electrolyte is improved. Each composite electrolyte showed stable cycling and good performance in an all-solid-state Li-metal battery with different cathodes. The good cycling performance of the all-solid-state cell with a cathode that can be inserted by the Li-salt anion benefits from the undesirable small Li^+ transference number of the composite electrolyte.

Results and Discussion

Li^+ transport in the composite electrolytes

The fluorite $Gd_{0.1}Ce_{0.9}O_{1.95}$ (GDC) and perovskite $La_{0.8}Sr_{0.2}Ga_{0.8}Mg_{0.2}O_{2.55}$ (LSGM) with an average particle size of 0.077 and 0.243 μm, respectively, are uniformly distributed in the dense and flexible composite polymer electrolytes (CPEs) (Figure S1). Oxygen-vacancy $(V_O^{\bullet\bullet})$ rich GDC[16] and LSGM[17] have oxygen conductivities of 1.9×10^{-2} and 3.4×10^{-3} S cm^{-1} at 600 °C, respectively. Figure 1 a and Figure S2a,b show X-ray diffraction patterns of the composite electrolytes (CPEs) with and without GDC and LSGM powders (CPE-xGDC or CPE-xLSGM, where x wt % is the weight percent of the GDC or LSGM powders). The peaks of the pristine GDC and LSGM powders match the peaks of the powders in the composite electrolytes, indicating their stability with PEO-LiTFSI. The two characteristic peaks at 19.15 and 23.35 degrees 2θ in the XRD pattern of PEO-LiTFSI electrolyte without a filler are from crystalline PEO, and the broad peak at 20 degree confirms the coexistence of crystalline and amorphous phases in the PEO/LiTFSI electrolyte.[9b] These

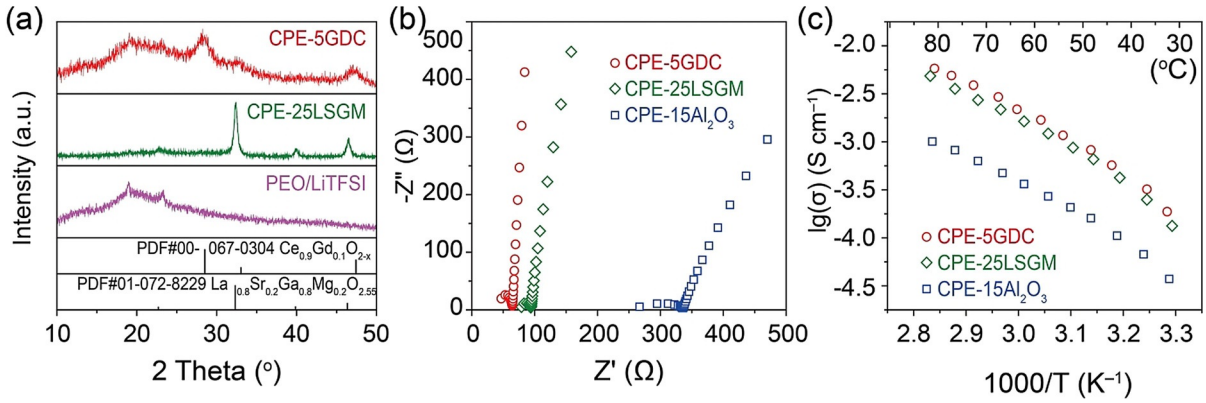

Figure 1. a) XRD patterns, b) impedance plots (30 °C), and c) Arrhenius plots of Li^+ conductivities of the composite electrolytes ([EO]/[Li] ratio $n=10$).

two small crystalline PEO peaks remained in the CPEs with 5 wt% GDC (CPE-5GDC) but disappeared in CPE-xGDC membranes with $x \geq 10$. The introduction of GDC and LSGM fillers as a solid plasticizer increased the segment motion of PEO chains at room temperature.

The introduction of a suitable amount of GDC and LSGM powders can improve Li^+ transfer in the PEO by increasing the amount of the amorphous phase in the polymer electrolyte. Figure 1c and Figure S2c,d showed the Arrhenius plots of Li^+ conductivities of the CPEs with varying amounts of GDC or LSGM powders. A CPE with 15 wt% nano-Al_2O_3 (CPE-15Al_2O_3), which has one order of magnitude higher Li^+ conductivity than that of the PEO-LiTFSI electrolyte,[10] is shown for comparison. The Li^+ conductivities of all the CPE-xGDC and CPE-xLSGM CPEs are higher than that of CPE-15Al_2O_3 from 30 to 80 °C. CPE-5GDC and CPE-25LSGM CPEs show the highest Li^+ conductivities for each filler of 1.9×10^{-4} and 1.3×10^{-4} S cm^{-1} at 30 °C with an activation energy of 0.26 and 0.28 eV from 30 to 80 °C, respectively. The electronic conductivity of these CPEs is about 5.5×10^{-10} S cm^{-1} (Figure S3). Increasing the concentration of GDC and LSGM powders increases the interfacial surface area between the powders and the polymer electrolytes, but reduces Li^+ conductivities (Figure S2c,d). This trend indicates the Li^+ conduction on the oxide/polymer interface does not contribute significantly to the total Li^+ conductivity in the composite electrolyte; the high concentration of powders dilute the polymer electrolyte and block Li^+-transfer in the polymer.

Local Li^+ environments and conduction mechanism in the composite electrolytes

The high Li^+ conductivity of the CPE-5GDC composite electrolyte with a mixed amorphous and crystalline phase indicates the oxygen conducting inorganic fillers have an effect on the Li^+ conduction in CPEs. High-resolution solid-state Li nuclear magnetic resonance (NMR) spectroscopy allowed the investigation of the local Li^+ environments and the mechanism of Li^+ conduction in these CPEs (Figure 2). Figure 2a shows the ^{7}Li MAS NMR spectra of three CPEs, each consisting of a different oxide filler (GDC, LSGM, and Al_2O_3) and an [EO]/[Li] ratio $n = 13$. Two peaks corresponding to two different Li^+ environments were identified by fitting the asymmetric peak in the NMR spectra. The Li ions related to the right peak (A1; colored red in the Figure) are trapped by the coordinated oxygen in PEO and have less of a contribution to the Li^+ conduction at room temperature; the left peak (A2; colored green in the Figure) originates from the more mobile Li^+ ions in PEO. The greater mobility of the Li^+ ions in the A2 site stems from greater local disorder and weaker interaction with the oxygen in PEO.[15b,c] Introduction of Al_2O_3, LSGM, or GDC increased the population of mobile Li^+ by 9.7%, 11.1%, and 14.5% in the A2 site, respectively, which is reflected in corresponding variances in the peaks of the NMR spectra. This result is in agreement with the enhancement of Li^+ conductivity observed in the EIS measurements (Figure 1b) and is further corroborated by the obtained ^{7}Li longitudinal T_1 relaxation times (Table S1). The values of ^{7}Li T_1 decreased (i.e., higher Li^+ mobility) when the PEO-LiTFSI matrix is infused with oxide fillers Al_2O_3 (0.48 s), LSGM (0.35 s), and GDC (0.25 s). In addition to the ^{7}Li T_1 times, a broadening linewidth for the A2-site peak for the mobile Li^+ in CPE(13:1)-5GDC qualitatively suggests that $V_O^{\bullet\bullet}$-enriched GDC is more effective in creating the disordered local Li^+ environment that is favorable for Li^+ conduction. The up-field shift of the ^{7}Li signal in CPE (13:1)-Al_2O_3 in Figure 2a indicates the introduction of Al_2O_3 increased the Li^+ conductivity by weakening the PEO–Li^+ interaction. However, the impedance spectra and ^{7}Li T_1 measurements suggest the down-field (higher ppm) shift of ^{7}Li signals in both the CPE(13:1)-25LSGM and CPE(13:1)-5GDC is owing to the nature of the oxygen vacancies in each structure rather than the increased PEO–Li^+ interaction.

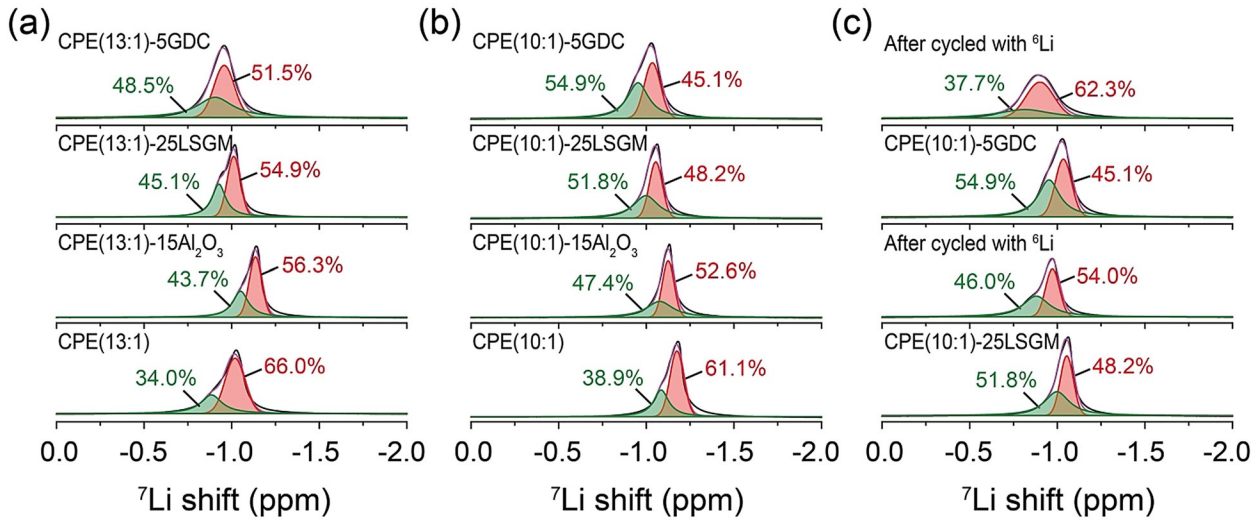

Figure 2. ^{7}Li MAS NMR spectra of the composite electrolytes with different [EO]/[Li] ratios a) $n = 13$, b) $n = 10$; c) ^{7}Li MAS NMR spectra of the composite electrolyte before/after ^{6}Li → ^{7}Li tracer-exchange experiment at room temperature.

Figure 2b shows the ^{7}Li MAS NMR spectra of CPEs consisting of one of three oxide fillers (GDC, LSGM, and Al_2O_3) with a [EO]/[Li] ratio $n = 10$. The LiTFSI concentration (from [EO]/[Li] ratio $n = 13$ to [EO]/[Li] ratio $n = 10$) show a negligible impact on modifying the local Li^+ environments when the PEO-LiTFSI matrix is dosed with the same wt% of LSGM/GDC (Figure 2b). Since the ^{7}Li chemical shifts in CPE(10:1)-5GDC and CPE(13:1)-5GDC (or in CPE(10:1)-25LSGM and CPE(13:1)-25LSGM) are almost identical ($\Delta_{GDC} = 0.072$ ppm; $\Delta_{LSGM} = 0.043$ ppm), the primary contribution to the observed ^{7}Li chemical shifts (i.e., different Li^+ local environment) stems from adding the insulating oxides (GDC/LSGM) with oxygen vacancies instead of being dominated by PEO–Li^+ interactions as has been previously reported in the literature.[18] 54.9% and 51.8% Li^+ ions are identified in the fast Li-conducting A2 environment for the CPE-5GDC and CPE-25LSGM composite electrolytes with [EO]/[Li] = 10 (Figure 2b), respectively. Increasing the LiTFSI concentration increased the Li^+_{A2}/Li^+_{A1} ratio as well as the total number of Li^+ ions in the A2 site causing Li^+ ions with greater mobility to participate in the Li^+ transport in CPEs. The CPEs with $n = 10$ showed a Li^+ conductivity an order of magnitude higher than that of the CPEs with $n = 13$ (Figure S4). As expected, the CPE(10:1) and the CPE(10:1)-15Al_2O_3 show a reduced ^{7}Li T_1 time. However, CPE(10:1)-GDC/LSGM electrolytes (Table S1) have longer ^{7}Li T_1 times than the CPE(13:1)-GDC/LSGM. This anomaly in the ^{7}Li T_1 times suggests that the increased density of mobile Li^+ ions in CPE(10:1)-GDC/LSGM along with the assistance from oxygen vacancies gives rise to liquid-like motion with longer ^{7}Li T_1 time behavior, which agrees with previous work.[19]

After identifying the positive effect of the O^{2-}–$V_O^{\bullet\bullet}$ interaction on Li^+ conductivity in the CPEs, we used ^{6}Li → ^{7}Li tracer-exchange NMR to verify the Li^+ transport pathway and explore the conduction mechanism in CPE(10:1)-LSGM/GDC. As shown in Figure 2c, the fraction of ^{7}Li signals (A2) significantly reduces (note decrease in intensity/height) in both the CPE(10:1)-LSGM/GDC after cycling with ^{6}Li electrodes. The more ^{7}Li that gets replaced with ^{6}Li in the CPEs during the tracer-exchange, the more mobile the Li^+ is in the corresponding environment that is responsible for conduction. This finding is consistent with our previous work.[15c] It should be noted that a significant reduction of ^{7}Li signal in the A2 site is revealed in CPE(10:1)-5GDC, suggesting that O^{2-}–$V_O^{\bullet\bullet}$ interaction in CPE(10:1)-5GDC is much stronger than that in CPE(10:1)-25LSGM, and ^{7}Li in CPE(10:1)-5GDC is much more easily replaced by ^{6}Li.

Density functional theory (DFT) calculations were performed to investigate the interaction between the surface of the GDC/LSGM/Al_2O_3 powders and the Li-salt in the polymer electrolytes. Three possible adsorption geometries for coordination of the TFSI ions to the surface of the fillers (SO_2 contact, CF_3 contact, and parallel contact) were calculated. The geometry with the SO_2 slab contact showed the largest adsorption energy (Figure S5). As illustrated in Figure 3, the $TFSI^-$ anions tend to bind to the surface of the crystal with the O attachment. The accumulation of the electrons between the O atom of $TFSI^-$ anion and the surface

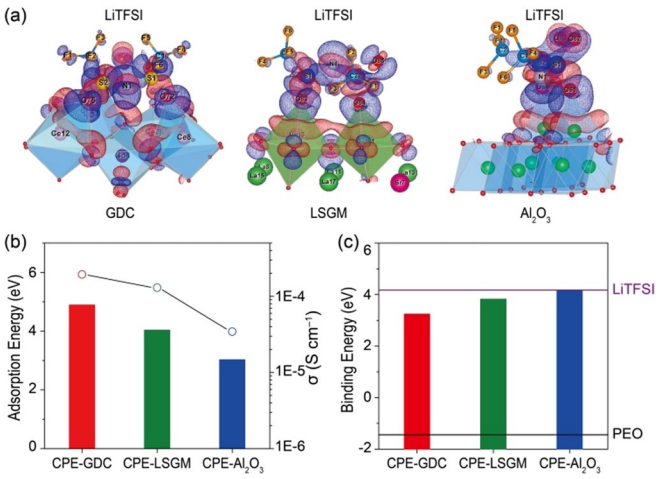

Figure 3. a) Calculated differential electron density distribution on the surface of GDC, LSGM, and Al_2O_3. Blue and red isosurface represent electron accumulation and depletion, respectively. b) $TFSI^-$ adsorption energy on the surface of the crystal and the corresponding experimental measured Li^+ conductivity. c) Calculated Li binding energy of the $TFSI^-$ adsorbed on each substrate surface, free $TFSI^-$ (purple), and free PEO (black).

of the crystal indicates the formation of a bond between the $TFSI^-$ anion and the surface of the inorganic filler, as shown in Figure 3a. All three surfaces show a strong binding with $TFSI^-$ anions; the GDC surface has the strongest $TFSI^-$ adsorption capability while the Al_2O_3 surface has the weakest $TFSI^-$ adsorption energy. This same trend is also seen with the experimentally measured Li^+ conductivity (Figure 3b). The Li^+ binding energy to the adsorbed $TFSI^-$ is also calculated and compared to the conventional LiTFSI binding energy (Figure 3c). The trend of Li^+–$TFSI^-$ binding energies corresponds well to our hypothesis; the stronger the $TFSI^-$ binding to the surface of the inorganic filler, the weaker it binds to the Li^+. The higher Li^+ transference number of CPE-5GDC (0.26) electrolyte than those of CPE-25LSGM (0.18) and CPE-15Al_2O_3 (0.13) electrolytes is also consistent with the result of the strongest $TFSI^-$ adsorption occurring on the GDC surface. The Li^+ transfer benefits in several ways from the adsorption of $TFSI^-$ on the surface of oxide particles by (1) reducing the Li^+–$TFSI^-$ interaction and releasing more Li^+, thus increasing the Li^+ transference number in the electrolyte, and (2) changing the Li^+ distribution, as shown in the NMR results. The introduction of the GDC filler decreased the Li^+ binding to the $TFSI^-$ anion the most, thus leading to the largest enhancement of the Li^+ transference number and Li^+ conductivity in the electrolyte. The binding energy of Li^+ on the adsorbed $TFSI^-$ in CPE-15Al_2O_3 (4.15 eV) is very similar to that of unbound free $TFSI^-$ (4.18 eV), limiting the enhancement of Li^+ transfer from the inorganic filler.

Fourier transform infrared spectroscopy (FTIR) was employed to analyze the ion-pairing of $TFSI^-$ anions and further elucidate the bonding between the $TFSI^-$ anions and the GDC/LSGM particles (Figure S6). The peak centered at 740 cm^{-1}, which corresponds to the S–N stretching of free $TFSI^-$ anions, is sensitive to ion pairing.[20] This peak did not

shift or broaden with the introduction of GDC/LSGM fillers, indicating that most of the lithium salt is dissociated in PEO. The small perturbation at 745 cm^{-1} comes from undissociated LiTFSI. The ratios of paired $TFSI^-$ anions in the CPE-25LSGM and CPE-5GDC are much higher than those of CPE-15Al_2O_3. The higher Li^+ conductivity of the CPEs with GDC and LSGM indicate that $TFSI^-$ anions are partially paired by the positively-charged oxygen vacancies on the surface of LSGM and GDC rather than the Li^+ ions in PEO.

Symmetric Li/Li cell with the composite electrolytes

A symmetric Li/CPE-5GDC/Li cell was cycled at 35 °C to investigate the compatibility of the composite electrolyte with a Li-metal anode. From a symmetric cell, the plating/stripping process of lithium, and the Li/composite electrolyte interface stability during cycling can be thoroughly investigated prior to evaluating performance in a full cell. Figure 4a shows the

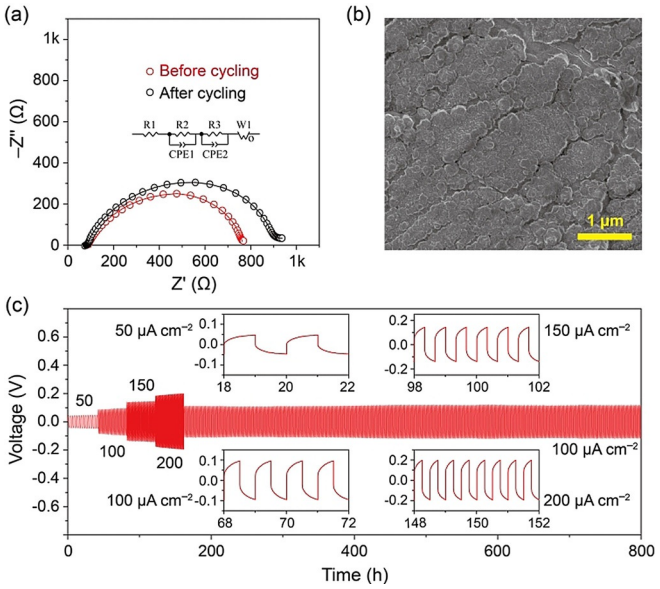

Figure 4. The symmetric Li/Li cell with CPE-5GDC composite electrolyte. a) The impedance plots of the Li/Li symmetric cell before and after cycling. b) SEM image of lithium metal surface after cycling. c) The cycling performance of the symmetric Li/Li cell with different current densities at 35 °C. The surface area of Li metal was 0.5 cm^2.

electrochemical impedance plots of the symmetric cell before and after cycling the cell at 35 °C for 800 h; the Li/CPE-5GDC interfacial resistance slightly increased from 163 to 185 Ω cm^2 after cycling. The symmetric cell (Figure 4c) showed stable cycling from 0.05 to 0.2 mA cm^{-2} for 800 h, indicating a stable Li/CPE-5GDC interface with the ability to suppress lithium-dendrite growth. The symmetric cell was disassembled after cycling to extract the lithium metal for examination of any morphological changes of lithium metal upon repeated long-term plating/stripping. Figure 4b shows that the surface of the Li metal after cycling is flat and does not show any evidence of lithium dendrite formation. The CPE-25LSGM composite electrolyte had comparable cycling performance to the CPE-5GDC composite electrolyte in the Li/Li symmetric cell (Figure S7).

All-solid-state Li-metal batteries with the composite electrolytes

All-solid-state Li-metal batteries with different cathodes, including $LiFePO_4$ (LFP), $LiNi_{0.8}Mn_{0.1}Co_{0.1}O_2$ (NMC), and a polyaniline organic cathode, were assembled to evaluate the electrochemical performance and stability of the composite electrolyte in an all-solid-state battery configuration. PEO/LiTFSI and PVDF/LiTFSI were added to the LFP and NMC cathode, respectively, to provide a matrix with Li^+ conductivity in the cathode. The all-solid-state Li/$LiFePO_4$ cell had a total resistance of 330 Ω at 35 °C (Figure S8) with a discharge capacity of 160 and 128 mAh g^{-1} at 100 and 300 μA cm^{-2}, respectively. The stability of CPE-5GDC up to 4 V (Figure S9) was confirmed with linear sweep voltammetry of a Li/CPE-5GDC/stainless steel cell.[21] We attribute the high coulombic efficiency (about 99%) and long cycle life performance to the superior stability of the CPE-5GDC composite in the operating voltage of the Li/LFP. The PVDF/LiTFSI electrolyte in the NMC cathode has a lower Li^+ conductivity (10^{-6} to 10^{-5} S cm^{-1}), but better electrochemical stability at high voltage (stable up to 4.8 V vs. Li^+/Li) than the PEO/LiTFSI electrolyte at 40 °C.[15c] The all-solid-state Li/NMC cell shows a total resistance of 460 Ω at 35 °C (Figure 5a), and the cell cycled from 2.8 to 4.3 V had a discharge capacity of 156, 135, and 108 mAh g^{-1} at 50, 100, and 150 μA cm^{-2}, respectively (Figure 5b). When the current density was changed back to 100 μA cm^{-2}, the capacity recovered with negligible decay (Figure 5c). The coulombic efficiency of the cell remained above 99% over 100 charge/discharge cycles while retaining a capacity of 100 mAh g^{-1}.

The small Li^+ transference number of the composite electrolyte represents the $TFSI^-$ anions having weak interactions with PEO are more mobile than the Li^+, which usually introduces a concentration polarization during cell cycling. To minimize the concentration polarization upon cycling in the all-solid-state setup, we opted for a polyaniline organic cathode into which $TFSI^-$ anions can insert. The ability of $TFSI^-$ anions to insert into the polyaniline effectively removes the concentration polarization that would otherwise present itself with a traditional lithium insertion cathode. The total resistance of the Li/CPE-5GDC/polyaniline cell is 280 Ω at 35 °C (Figure 5d). The $TFSI^-$ anions inserted into the polyaniline during charge, and were extracted back into electrolyte during discharge.[22] Figure 5e shows the sloping charge/discharge voltage curve resulting from the reversible insertion/extraction of the $TFSI^-$. The cell showed a good rate performance with a discharged capacity of 110, 105, and 80 mAh g^{-1} at 50, 100, and 200 μA cm^{-2}, respectively. Stable cycling for 160 cycles with a high coulombic efficiency of 99.5% is demonstrated in Figure 5f.

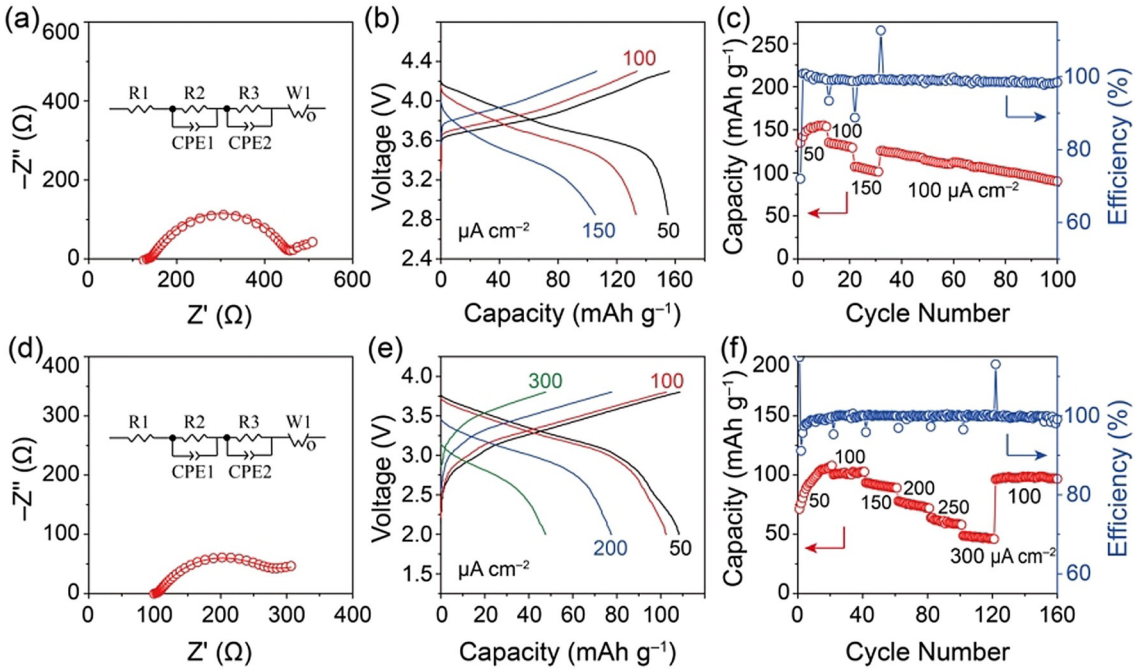

Figure 5. All-solid-state Li/NMC cell cycled at 35 °C. a) Electrochemical impedance plots, b) charge/discharge voltage profiles, and c) capacity retention and cycling efficiency. All-solid-state Li/polyaniline cells cycled at 35 °C. d) Electrochemical impedance plots, e) charge/discharge voltage profiles, and f) capacity retention and cycling efficiency. (The area of the cathodes and Li metal were 0.3 and 0.5 cm^2, respectively.)

Conclusion

In summary, the strong interaction between the surface oxygen vacancies of GDC/LSGM and the $TFSI^-$ anions in the composite polymer electrolyte changes the Li^+ distribution in two local environments. The increase of mobile Li^+ ions in A2 significantly enhances the Li^+ conductivity of the composite electrolyte, allowing for an all-solid-state Li-metal battery cells that cycles well at a reduced temperature. The low Li^+ transference number of the composite electrolyte is advantageous for an all-soild-state cell with a cathode that allows for the insertion of the Li-salt anion from the composite electrolyte.

Acknowledgements

N.W. thanks the China Scholarship Council for the opportunity to work in Texas. This work is supported by the Assistant Secretary for Energy Efficiency and Renewable Energy, Office of Vehicle Technologies of the U.S. Department of Energy through the Advanced Battery Materials Research (BMR) Program (Battery500 Consortium) award number DE-EE0007762. P.-H.C. and Y.-Y.H. acknowledge the financial support from National Science Foundation under Grant No. DMR-1808517. All solid-sate NMR experiments were performed at the National High Magnetic Field Laboratory. The National High Magnetic Field Laboratory is supported by National Science Foundation through NSF/DMR-1644779 and the State of Florida. Y.L. also acknowledges the funding support from TAFEL UTA18-000175.

Conflict of interest

The authors declare no conflict of interest.

Keywords: all-solid-state battery · composite electrolyte · Li-ion conductivity · Li-ion transfer mechanism · solid-state NMR

How to cite: *Angew. Chem. Int. Ed.* **2020**, *59*, 4131 – 4137
Angew. Chem. **2020**, *132*, 4160 – 4166

[1] a) J. B. Goodenough, K.-S. Park, *J. Am. Chem. Soc.* **2013**, *135*, 1167 – 1176; b) L. A.-W. Ellingsen, C. R. Hung, G. Majeau-Bettez, B. Singh, Z. Chen, M. S. Whittingham, A. H. Strømman, *Nat. Nanotechnol.* **2016**, *11*, 1039; c) L. Yue, J. Ma, J. Zhang, J. Zhao, S. Dong, Z. Liu, G. Cui, L. Chen, *Energy Storage Mater.* **2016**, *5*, 139 – 164.

[2] a) A. Manthiram, X. Yu, S. Wang, *Nat. Rev. Mater.* **2017**, *2*, 16103; b) J. Liu, Z. Bao, Y. Cui, E. J. Dufek, J. B. Goodenough, P. Khalifah, Q. Li, B. Y. Liaw, P. Liu, A. Manthiram, Y. S. Meng, V. R. Subramanian, M. F. Toney, V. V. Viswanathan, M. S. Whittingham, J. Xiao, W. Xu, J. Yang, X.-Q. Yang, J.-G. Zhang, *Nat. Energy* **2019**, *4*, 180 – 186.

[3] C. Sun, J. Liu, Y. Gong, D. P. Wilkinson, J. Zhang, *Nano Energy* **2017**, *33*, 363 – 386.

[4] a) R. Murugan, V. Thangadurai, W. Weppner, *Angew. Chem. Int. Ed.* **2007**, *46*, 7778 – 7781; *Angew. Chem.* **2007**, *119*, 7925 – 7928; b) Y. Li, J.-T. Han, C.-A. Wang, H. Xie, J. B. Goodenough, *J. Mater. Chem.* **2012**, *22*, 15357 – 15361.

[5] a) P. Adeli, J. D. Bazak, K. H. Park, I. Kochetkov, A. Huq, G. R. Goward, L. F. Nazar, *Angew. Chem. Int. Ed.* **2019**, *58*, 8681 – 8686; *Angew. Chem.* **2019**, *131*, 8773 – 8778; b) H.-J. Deiseroth, S.-T. Kong, H. Eckert, J. Vannahme, C. Reiner, T. Zaiß, M.

Schlosser, *Angew. Chem. Int. Ed.* **2008**, *47*, 755 – 758; *Angew. Chem.* **2008**, *120*, 767 – 770.
[6] T. Asano, A. Sakai, S. Ouchi, M. Sakaida, A. Miyazaki, S. Hasegawa, *Adv. Mater.* **2018**, *30*, 1803075.
[7] a) Y. Li, X. Chen, A. Dolocan, Z. Cui, S. Xin, L. Xue, H. Xu, K. Park, J. B. Goodenough, *J. Am. Chem. Soc.* **2018**, *140*, 6448 – 6455; b) Y. Li, W. Zhou, X. Chen, X. Lü, Z. Cui, S. Xin, L. Xue, Q. Jia, J. B. Goodenough, *Proc. Natl. Acad. Sci. USA* **2016**, *113*, 13313.
[8] a) M. B. Armand, *Annu. Rev. Mater. Sci.* **1986**, *16*, 245 – 261; b) W. H. Meyer, *Adv. Mater.* **1998**, *10*, 439 – 448; c) H.-K. Yoon, W.-S. Chung, N.-J. Jo, *Electrochim. Acta* **2004**, *50*, 289 – 293; d) H. Duan, Y.-X. Yin, Y. Shi, P.-F. Wang, X.-D. Zhang, C.-P. Yang, J.-L. Shi, R. Wen, Y.-G. Guo, L.-J. Wan, *J. Am. Chem. Soc.* **2018**, *140*, 82 – 85.
[9] a) K. Pożyczka, M. Marzantowicz, J. R. Dygas, F. Krok, *Electrochim. Acta* **2017**, *227*, 127 – 135; b) M. Marzantowicz, J. R. Dygas, F. Krok, J. L. Nowiński, A. Tomaszewska, Z. Florjańczyk, E. Zygadło-Monikowska, *J. Power Sources* **2006**, *159*, 420 – 430; c) M. Marzantowicz, F. Krok, J. R. Dygas, Z. Florjańczyk, E. Zygadło-Monikowska, *Solid State Ionics* **2008**, *179*, 1670 – 1678.
[10] F. Croce, G. B. Appetecchi, L. Persi, B. Scrosati, *Nature* **1998**, *394*, 456 – 458.
[11] S. Skaarup, K. West, B. Zachau-Christiansen, *Solid State Ionics* **1988**, *28 – 30*, 975 – 978.
[12] J. Zheng, M. Tang, Y.-Y. Hu, *Angew. Chem. Int. Ed.* **2016**, *55*, 12538 – 12542; *Angew. Chem.* **2016**, *128*, 12726 – 12730.
[13] P. Zhu, C. Yan, M. Dirican, J. Zhu, J. Zang, R. K. Selvan, C.-C. Chung, H. Jia, Y. Li, Y. Kiyak, N. Wu, X. Zhang, *J. Mater. Chem. A* **2018**, *6*, 4279 – 4285.
[14] a) L. Chen, Y. Li, S.-P. Li, L.-Z. Fan, C.-W. Nan, J. B. Goodenough, *Nano Energy* **2018**, *46*, 176 – 184; b) K. Fu, Y. Gong, J. Dai, A. Gong, X. Han, Y. Yao, C. Wang, Y. Wang, Y. Chen, C. Yan, Y. Li, E. D. Wachsman, L. Hu, *Proc. Natl. Acad. Sci. USA* **2016**, *113*, 7094; c) J. Wan, J. Xie, X. Kong, Z. Liu, K. Liu, F. Shi, A. Pei, H. Chen, W. Chen, J. Chen, X. Zhang, L. Zong, J. Wang, L.-Q. Chen, J. Qin, Y. Cui, *Nat. Nanotechnol.* **2019**, *14*, 705 – 711; d) H. Xu, P.-H. Chien, J. Shi, Y. Li, N. Wu, Y. Liu, Y.-Y. Hu, J. B. Goodenough, *Proc. Natl. Acad. Sci. USA* **2019**, *116*, 18815; e) X. Zhang, J. Xie, F. Shi, D. Lin, Y. Liu, W. Liu, A. Pei, Y. Gong, H. Wang, K. Liu, Y. Xiang, Y. Cui, *Nano Lett.* **2018**, *18*, 3829 – 3838; f) J. Zheng, Y.-Y. Hu, *ACS Appl. Mater. Interfaces* **2018**, *10*, 4113 – 4120; g) W. Liu, S. W. Lee, D. Lin, F. Shi, S. Wang, A. D. Sendek, Y. Cui, *Nat. Energy* **2017**, *2*, 17035; h) W. Liu, N. Liu, J. Sun, P.-C. Hsu, Y. Li, H.-W. Lee, Y. Cui, *Nano Lett.* **2015**, *15*, 2740 – 2745.
[15] a) Z. Xue, D. He, X. Xie, *J. Mater. Chem. A* **2015**, *3*, 19218 – 19253; b) Y. Dai, S. Greenbaum, D. Golodnitsky, G. Ardel, E. Strauss, E. Peled, Y. Rosenberg, *Solid State Ionics* **1998**, *106*, 25 – 32; c) N. Wu, P.-H. Chien, Y. Li, A. Dolocan, H. Xu, B. Xu, N. S. Grundish, H. Jin, Y.-Y. Hu, J. B. Goodenough, *J. Am. Chem. Soc.* **2020**, http://doi.org/10.1021/jacs.9b12233.
[16] R. O. Fuentes, R. T. Baker, *J. Power Sources* **2009**, *186*, 268 – 277.
[17] T.-Y. Chen, K.-Z. Fung, *J. Eur. Ceram. Soc.* **2008**, *28*, 803 – 810.
[18] J. Zheng, H. Dang, X. Feng, P.-H. Chien, Y.-Y. Hu, *J. Mater. Chem. A* **2017**, *5*, 18457 – 18463.
[19] J. Adebahr, M. Forsyth, D. R. MacFarlane, P. Gavelin, P. Jacobsson, *J. Mater. Chem.* **2003**, *13*, 814 – 817.
[20] A. Bakker, S. Gejji, J. Lindgren, K. Hermansson, M. M. Probst, *Polymer* **1995**, *36*, 4371 – 4378.
[21] F. Chen, D. Yang, W. Zha, B. Zhu, Y. Zhang, J. Li, Y. Gu, Q. Shen, L. Zhang, D. R. Sadoway, *Electrochim. Acta* **2017**, *258*, 1106 – 1114.
[22] H. Gao, L. Xue, S. Xin, J. B. Goodenough, *Angew. Chem. Int. Ed.* **2018**, *57*, 5449 – 5453; *Angew. Chem.* **2018**, *130*, 5547 – 5551.

Manuscript received: November 13, 2019
Accepted manuscript online: December 31, 2019
Version of record online: January 23, 2020

